

See discussions, stats, and author profiles for this publication at: <https://www.researchgate.net/publication/26234662>

# Atomic Mechanisms Governing the Elastic Limit and the Incipient Plasticity of Bending Si Nanowires

ARTICLE *in* NANO LETTERS · JULY 2009

Impact Factor: 13.59 · DOI: 10.1021/nl9012425 · Source: PubMed

---

CITATIONS

45

READS

38

## 8 AUTHORS, INCLUDING:



Lihua Wang

Beijing University of Technology

25 PUBLICATIONS 354 CITATIONS

[SEE PROFILE](#)



Yuefei Zhang

Beijing University of Technology

94 PUBLICATIONS 2,791 CITATIONS

[SEE PROFILE](#)



Zhaoyong Zhang

Edith Cowan University

280 PUBLICATIONS 3,213 CITATIONS

[SEE PROFILE](#)

# Atomic Mechanisms Governing the Elastic Limit and the Incipient Plasticity of Bending Si Nanowires

Kun Zheng, Xiaodong Han,\* Lihua Wang, Yuefei Zhang, Yonghai Yue, Yan Qin, Xiaona Zhang, and Ze Zhang\*

Institute of Microstructure and Properties of Advanced Materials, Beijing University of Technology, Beijing, 100124, China

Received April 19, 2009

## ABSTRACT

Individual single-crystalline Si nanowires (NWs) were bent by forming loops or arcs with different radius. Positional-resolved atomic level strain distribution (PRALSD) along both of the radial and axial directions were calculated and mapped directly from the atomic-resolution strained high-resolution electron microscopy (HREM) images of the bent Si NWs. For the first time, the neutral-strain axis shifted from the compressive zone to the tensile region was directly demonstrated from the PRALSD along the radial direction. Bending-induced ripple-buckling of the bent Si NW was observed and a significant strain variation along the bending axial direction in the compressive region was revealed. The tensile surface atomic steps and the compressive buckling are the physical origin of the asymmetric tensile-compressive properties of postelastic instabilities and the incipient plasticity. Both of the tensile surface atomic-steps and the compressive buckling initiated versatile ductile plastic dislocation events.

Si nanowires (NWs) are one of the most important one-dimensional nanomaterials<sup>1</sup> to build nanodevices<sup>2–4</sup> since its successful fabrication in 1998.<sup>5,6</sup> They also show unusual giant piezo-resistance phenomena under stress.<sup>7</sup> In the bendable electronics<sup>8</sup> and those of nanogenerators,<sup>9–11</sup> the nanowires' elastic limits and the intrinsic characters of postelastic transformation are extremely important for applying these materials under stress. Bulk silicon (Si) and other semiconductor materials usually exhibit brittleness at low temperature due to their high Peierls stress for activating the dislocation nucleation and/or motion. Usually, only at an appreciable fraction of their melting point, dislocations can be activated and they can become ductile. It has been reported for over more than one decade that the necessary temperature for triggering plasticity of bulk Si under stress was at least 400 °C.<sup>12</sup> That is to say, room-temperature-plasticity hardly happens for bulk Si. However, when the materials' size goes down to small scale, the defect-free structure normally makes the nanomaterials survive with high fracture stresses,<sup>13–15</sup> and this could eventually allow the materials to have chances to overcome the critical resolved shear stresses and nucleate ductile dislocations or make these ductile featured dislocations mobile. The fracture and deformation characters of the nanomaterials can be significantly different from those of bulks. Although many researches on mechanical properties

of semiconductor NWs have been reported,<sup>16–19</sup> very limited information about the atomic structure evolving process for semiconductor NWs under applied stress were available and most of the mechanisms rely on computer simulations.<sup>20–23</sup> The establishment of a comprehensive and direct understanding on an atomic-level of the mechanisms behind the fascinating behaviors of one-dimensional nanomaterials has long been a challenge but has been highly desirable. In a previous study,<sup>24</sup> we in situ investigated the tensile properties of Si NWs using a simple and effective method in a transmission electron microscope (TEM). Employing the similar technique here, for the first time we report the direct atomic mechanisms of the onset plasticity of bending Si NWs in which both of the tensile and compressive stress were simultaneously applied on the Si NWs. The gradient tensile-compressive stress-induced asymmetric elastic-plastic transitions of Si NWs were revealed. The atomic mechanisms of these processes were demonstrated directly under high-resolution TEM (HREM).

A thermal evaporation technique was employed to fabricate the Si nanostructures. The morphology and characterization of Si NWs are shown in Figure 1. Figure 1a provides low-magnified scanning electron microscope (SEM) morphology of Si NWs. These high-quality Si NWs have uniform diameter with about 30–50 nm and length above several tens of micrometers. The typical example morphology of a Si NW is shown in Figure 1b. Figure 1c is the corresponding

\* To whom correspondence should be addressed. E-mail: (X.H.) xdh@bjut.edu.cn; (Z.Z.) zezhang@bjut.edu.cn.

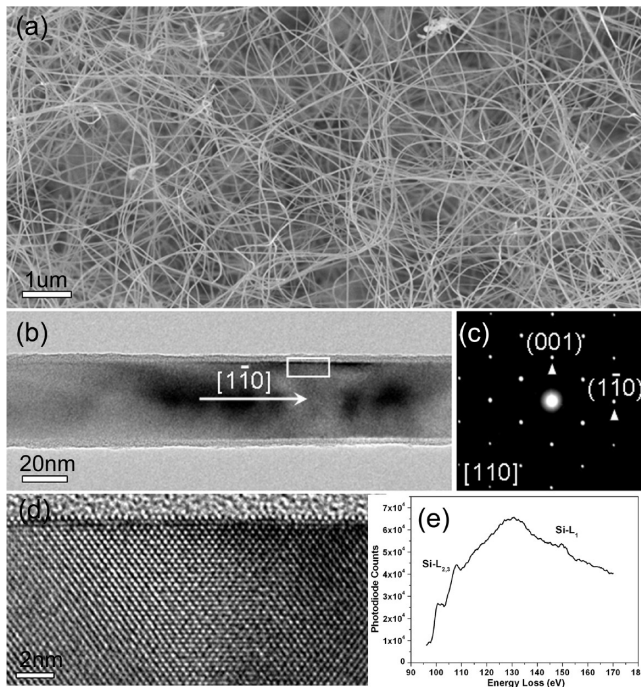


**Figure 1.** The synthesized Si NWs. (a) The morphology of Si NWs under SEM observation; (b) TEM image of an individual Si NW; (c) the corresponding SAEDP which shows the longitude orientation of Si NW is  $[1\bar{1}0]$ ; (d) HREM images taken from the white framed region of (b). (e) EELS spectrum showing the  $L_{2,3}$  edge character of a Si NW.

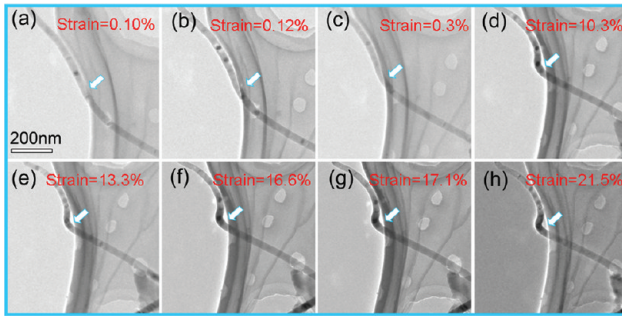


**Figure 2.** (a–h) A series of low-magnified TEM images of a continuous bent process of a single Si NW; see text for details.

selected area electron diffraction pattern (SAEDP) that shows that the longitude orientation of Si NW is  $[1\bar{1}0]$ . Figure 1d is the enlarged HREM image of the Si NW taken from the white framed region of Figure 1b. Atomic scale smooth surface can be demonstrated. The electron energy-loss spectrometry (EELS) spectrum (Figure 1e) showing the  $L_{2,3}$  edge character of Si NWs indicates that the synthesized material is high quality Si NWs.

The in situ bending deformation of Si NWs were carried out in an HREM via mechanical force created by the TEM specimen supporting colloidal thin film under the irradiation of electron beam as reported in details elsewhere.<sup>24–26</sup> Figure 2a–h shows a continuous bending process of a single Si NW bent by the supporting colloidal thin film. The bent point was indicated by arrows. The bent strain sustained in the bent Si NW increased from 0.1% as shown in Figure 2a to be about 21.5% as shown in Figure 2h. (The traditional

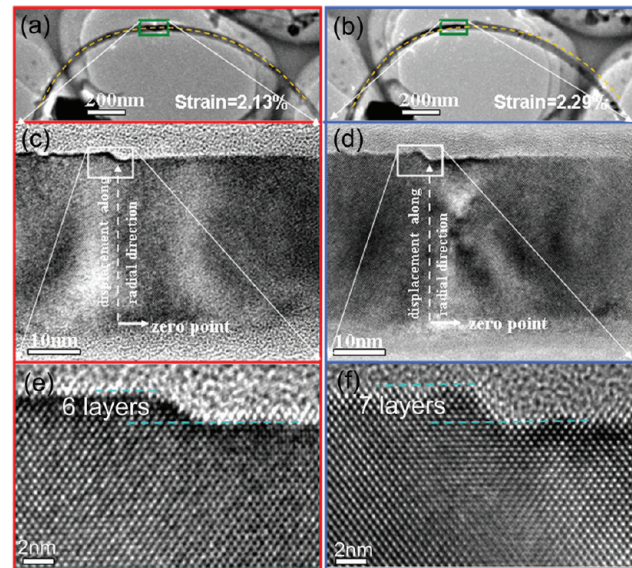


**Figure 3.** A single Si NW bent process was shown at atomic scale. (a,b) Low-magnified TEM images captured at a time interval about 400 s with the bent strain increased from 2.13 to 2.29%. (c,d) Enlarged images taken from the green framed regions of (a) and (b), respectively. (e,f) HREM images taken from the white framed regions of (c,d), respectively. The HREM images show the surfaces steps increased from six atomic layers to seven.

method was used to calculate the strain of the bending Si NW according to the formula  $\varepsilon_{\text{elastic}} = r/(r + R)\%$ ,<sup>25,27</sup> where  $R$  is the bending curvature, and  $r$  is the radius of crystal Si NW.) Finally, the bending angle of the bent Si NW almost approached  $90^\circ$  and the calculated local strain was above 21.5%. With such a high bent strain, the Si NW survived without abrupt fractured failure. Complicated elastic and plastic mechanical deformation process was involved in this bent. However, in this research we will focus on the incipient plastic behavior of bending Si NWs other than the exhausted plasticity limit of the bent Si NWs.

Because the special structure of surfaces, the Si–Si bonds at the surfaces could become weak.<sup>28</sup> Particularly in the bending process, the surface at the tensile side tolerates the largest tensile strain and therefore, the postelastic instability events should prefer to happen at the surfaces by either plastic dislocations or brittle cracks. Figure 3 shows a Si NW bending process at the atomic scale. Figure 3a,b shows low-magnified TEM images captured at a time interval about 400 s. According to the same reference (the yellow dashed line) shown in Figure 3a,b, it was revealed that the average bent strain increased from 2.13% (Figure 3a) to be about 2.29% (Figure 3b). From the enlarged images (Figure 3e,f), which were taken from the white framed regions of Figure 3c,d, it can be clearly seen that the surface steps increased from six atomic layers to seven. The strain for inducing this one-atomic layer surface step is about 0.16%. The tensile surface steps were possibly derived from a perfect dislocation on the  $(111)$  plane with a shuffle feature.<sup>29</sup> At this slow deformation rate, we did not see a crack-initiated failure when exceeding its elastic limit.

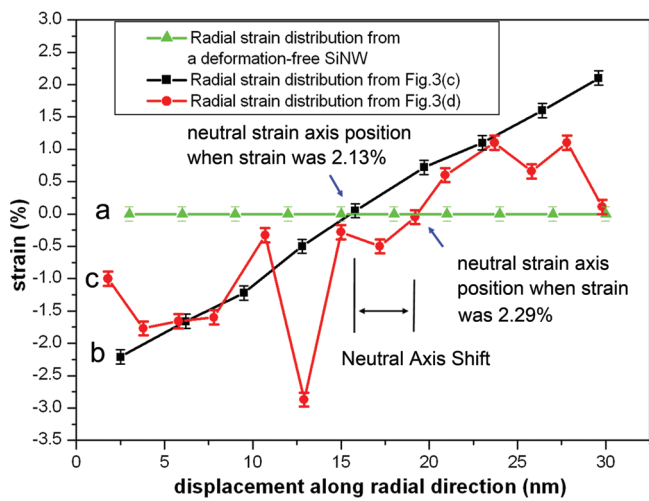


**Figure 4.** Strain distribution along the radial direction of the bent Si NW. The green triangle-line shows the strain distribution of the deformation-free Si NW; the black square-line shows the strain distribution along the line shown in Figure 3c; the red dot-line shows the strain distribution along the line shown in Figure 3d. See text for details.

When a nanowire is under bending, the tensile region versus compressive region can have significant and distinctive mechanical and electrical response at the nano and atomic scale.<sup>9–11,30,31</sup> It is particularly significant to realize and understand the accurate atomic-scale structural evolution of the continue-bending-stressed nanowires. Using our recent developed techniques,<sup>24,25</sup> the bent-strained nanowires can be double-titled along a pair of orthogonal axes by large angles ( $\pm 30^\circ$ ). This flexibility allows observing the strained-nanowires along any low Miller index axis and achieving atomic-resolution imaging easily. We thus are able to measure the strained-lattice-distance (SLD) of  $d_{110}$  and

calculated the strain distribution along the nanowire's radial direction of the bent nanowire. The strain  $\varepsilon_{110}$  of (110) plane can be calculated by normalizing the measured SLD values from the direct atomic-resolution HREM imaging ( $\varepsilon_{110} = (d_{110}Z - d_{110}R)/d_{110}R$ ),  $d_{110}Z$  is the lattice distance at a position  $Z$  of the bent Si NW and  $d_{110}R$  is the (110) lattice distance of the reference Si lattice of the undeformed Si NW (see Supporting Information). The positional-resolved atomic level strain distributions (PRALSD) along both of the axial and radial directions can thus be provided. Because of the case of bending, the strain along the radial direction can be aggressively different and a neutral-strain line normally exists along the central axis of the bent wire. The highly strained lattice distance of the bent Si NW can be directly measured along both of the radial and the axial directions with different bending stains. Normalized by the lattice-spacing values of the unbent Si NW, these strain values were shown in Supporting Information, Table S1 and S2. These values revealed that the bending strains along both of the radial and axial directions are inhomogeneous. These values were plotted in Figures 4, 5, and 6, respectively, for revealing the bending-induced strain redistribution in the bent NW at atomic scale.

Figure 4 shows the strain distribution along the radial direction for the bent Si NW shown in Figure 3c,d. The PRALSD was obtained along the lines shown in Figure 3c,d, respectively. The abscissa-axis represents the measured distance from the bottom surface along radial direction (the bottom surface is defined as zero) in the HREM image shown in Figure 3c. The y-axis is the positional resolved strain (PRS) values along those positions. The selected positions are shown in Figure S3 (see Supporting Information). The green triangle-line “a” in Figure 4a shows the zero-strain line of the deformation-free Si NW and it served as a

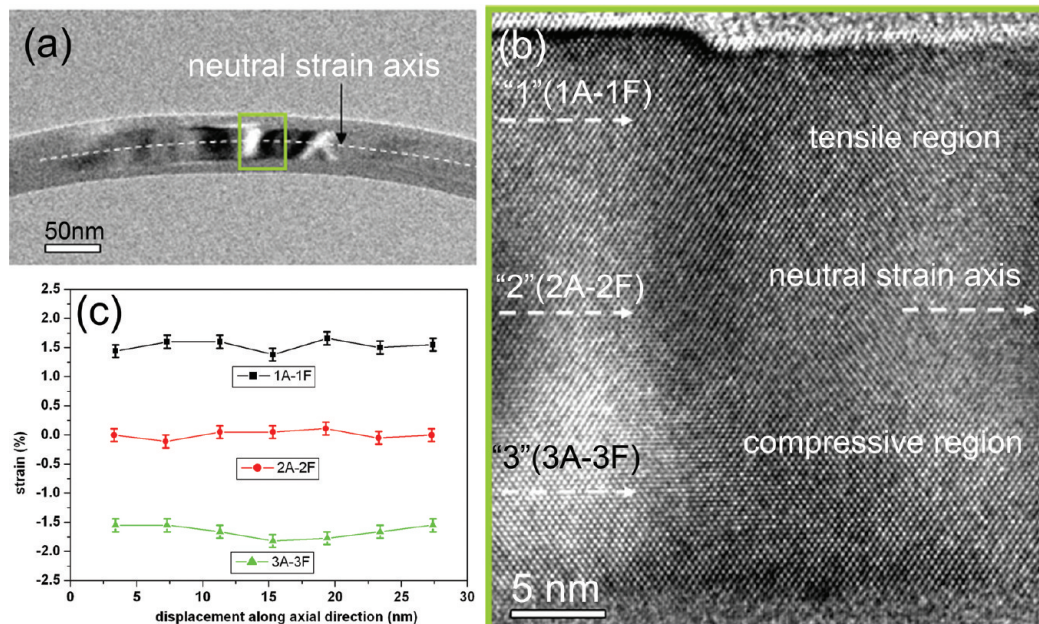


**Figure 5.** Strain distribution along the axial direction of the bent Si NW with 2.13% strain. (a) The low-magnified TEM image of the bent Si NW. The dashed line shows the neutral strain line. (b) HREM taken from the green framed region of (a). Three measured lines were indicated as “1”, “2”, and “3”. (c) The measured strains along 1, 2, and 3 lines show small fluctuates. See text for details.

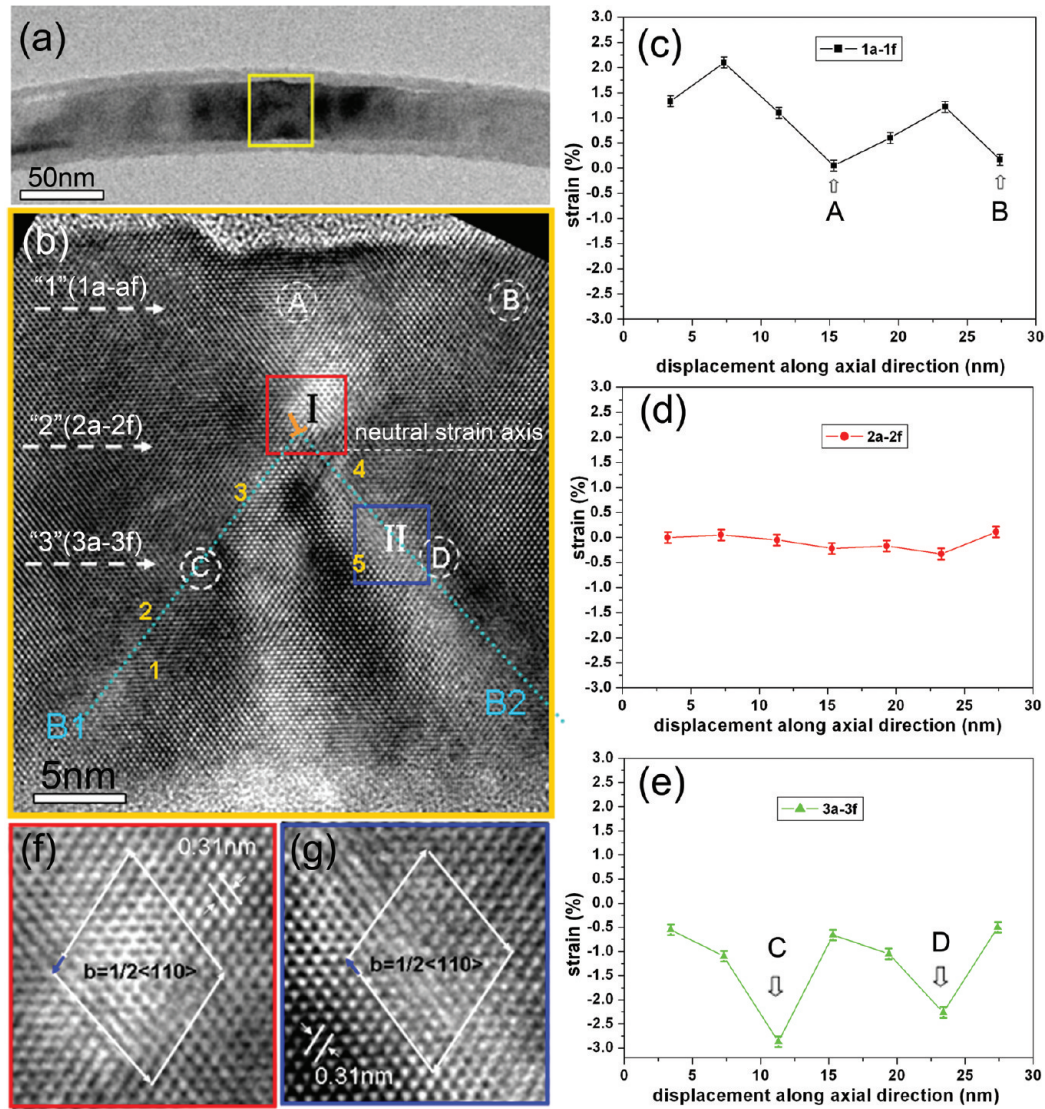


**Figure 6.** Strain distribution along the axial direction of the bent Si NW with 2.29% strain. (a) The low-magnified TEM of the bent Si NW. (b) HREM taken from the yellow region of (a). Three measured lines were also indicated as “1”, “2”, and “3”. (c–e) The measured strains along 1, 2, and 3 lines, respectively. (f,g) Enlarged from the regions “I” and “II” of (b) showing the details of dislocations. See text for details.

reference. The black square-line “b” was measured through the line shown in Figure 3c and it shows a typical linear strain increasing of a bending wire across the diameter. The strain line “b” in Figure 4 demonstrated the effectiveness and the sensitivity of the PRALSD method. The strain along the strain line “b” in Figure 4 evolved to be zero along the radial direction at the position of 15 nm from the bottom-surface and it roughly locates at the neutral-strain axis of tensile versus compressive stress. The largest strains were 2.2% for both of tensile and compressive surfaces. The line-strain distribution along the radial direction of the elastic bent Si NW in Figure 3c agrees with the theoretical description.<sup>27</sup> When the deformation strain continued to increase from Figure 3 panel c to panel d, the line-strain across the radial direction of the strained NW changed. As shown in Figure 4, the red dot-line “c”, which was taken from the line shown in Figure 3d, shows a wavy character other than a linear feature. In this strain-line, the zero-strain point roughly locates at the position of  $x = 19$  nm and it

obviously shifted to the tensile side of the bent NW. This is the first time direct observation that the bent Si NW shifts its neutral-strain axis to the tensile side. The wavy character of the strain line reflects the abrupt change of lattice spacing or strain-field introduced. The sharp increasing of the compressive strain indicated by character “E” of line “c” in Figure 4 came from the buckled-belt which will be discussed in the following section.

In addition to the PRALSD along the radial direction, the positional resolved strain distribution along the axial direction needs to be studied carefully to reveal the possible significant postelastic instability events. We measured the SLD values and calculated the PRALSD along the axial direction for the continuously bent Si NW shown in Figure 3c,d (i.e., the bending strain increased from 2.13% to be about 2.29%). As indicated in Figure 5b, three line-strains were calculated for the bent Si NW. Line 1 is located at the tensile strain region, line 2 is at about the neutral strain axis, and line 3 sits at the compressive zone. The strain distributions were

plotted for the 1, 2, and 3 lines in Figure 5c, respectively. Figure 5c indicated that all the measured line-strains along 1, 2, and 3 lines show small fluctuations though their absolute values vary significantly. No obvious plastic events happened for bending the Si NW at the moment of Figure 3c and it is consistent with the radial strain distribution as shown in Figure 4b. With increasing the bending strain to be about 2.29%, the axial strain distribution changes aggressively. A selected area in Figure 6a was enlarged and shown in Figure 6b, and the strains were also measured along three lines 1, 2, and 3 of the axial direction of the bent Si NW. Except for the neutral-strain line 2 that shows a flat strain distribution along the axial direction as shown in Figure 6d, the other two strain-lines along the axial direction show large fluctuations. Figure 6c shows two tensile strain valleys (indicated by A and B in Figure 6c). These two valleys locate at A and B as shown in Figure 6b; they are indicators of strain-release after emitting dislocation. Figure 6e shows two compressive strain peaks (negative strain values) as indicated by C and D. C and D are indicated in Figure 6b. C and D are 3 nm far from their dislocation neighbor zones, and they sit on the strain-belts as indicated by B1 and B2 in Figure 6b. The two strain-belts form a “ $\Lambda$ ” shape and it is a reflection of strain/stress gradient along the radial direction. These compressive strain-belts are ripple-buckles, which are a typical feature of postelastic instabilities of nanotubes<sup>30</sup> or fibers.<sup>31</sup> As indicated by 1, 2, 3, 4, and 5, multiple dislocations located at or close to the two ripple-buckles are indicated. From the atomic-scale direct observations, we conclude that these buckle-featured postelastic instabilities contain significant plastic dislocation events. A dislocation shown as the character “T” is indicated in Figure 6b, and it sits at the neutral-strain line and the cross-point of the two compressive ripple-buckle belts. The dislocation “T” has strong strain-field and it affected the lattices above it in the tensile-stress region. The dislocation “T” is possible that the step-dislocation slipped over to the neutral-strain zone but it cannot slip across to the compressive side. Ripple-buckling has been reported for carbon nanotubes and carbon fibers by bending due to the distinctive in-plane and out-of-plane bonds structures (covalence bonds versus the van der Waals). However, it has never been reported that a solid cylinder like Si nanowire (with pure covalence bonds) can have this type of atomic scale ripple-buckles under compressive stress. This type of nanoscale ripple-buckling is distinctive with the Euler buckling that was reported in a previous research for Si NWs.<sup>18</sup>

Dislocation activities are the main initial postelastic events of bending Si NWs. Two framed areas were selected in Figure 6b and they are enlarged and shown in Figure 6f,g. Both areas contain a dislocation. The Burgers vector circuits were drawn to determine the dislocation type. The projection of the Burgers vectors of the two dislocation are with  $b = 1/2 [110]$ . Through the analysis of these HREM images, dislocations are the only plastic events. In our HREM results, no partial dislocation was found. It is well known that a glide 60° dislocation usually dissociates into two partial dislocations in order to reduce the activation energy, while a shuffle

60° dislocation cannot dissociate.<sup>32</sup> Then it is reasonable to deduce that these undissociated perfect 60° dislocations belong to shuffle sets. Retrieving the previous investigation results of the axial tensile tests on Si NWs<sup>24</sup> in which a phase transformation from single crystal to amorphous (c-a) structure happened, we can conclude that the dislocation activity happens prior to the c-a phase transition. The c-a phase transition could occur with a higher external stress with a direct c-a transition or on a highly distorted or dislocated matrix.

In summary, with the newly developed colloidal thin film technique, individual Si NWs were bent and the direct atomic-resolution processes of the structural evolution were investigated *in situ* by HREM. The direct demonstration of the asymmetrical mechanical response of tensile versus compressive stresses under bending is important for understanding not only the nanowire’s pure mechanical stabilities, but also the correlated mechanical-electrical coupling events, for example, the ZnO nanogenerators and flexible electronic devices. Attention should be paid to the fact that the mechanical response of the Si NWs under external force depends on the deformation rates. The earlier investigation on bending Si NWs that revealed brittle characters<sup>18</sup> of Si NWs under SEM observation should happen in a much faster strain rate.

**Acknowledgment.** This work was supported by National Excellent Young Scientist Foundation (10825419), Key Project of NSF of China (50831001), and Chinese National 973 program (2009CB623700). X.D.H. was also supported by the NCET (05009015200701) and Key Project Funding of Beijing Education Committee (JB102001200801).

**Supporting Information Available:** This material is available free of charge via the Internet at <http://pubs.acs.org>.

## References

- (1) Lieber, C. M. *MRS Bull.* **2003**, *28*, 486–491.
- (2) Cui, Y.; Lieber, C. M. *Science* **2001**, *291*, 851–853.
- (3) Huang, Y.; Duan, X.; Cui, Y.; Lauhon, L.; Lieber, C. L. *Science* **2001**, *294*, 1313–1317.
- (4) Tian, B.; Zheng, X.; Kempa, T. J.; Fang, Y.; Yu, N.; Yu, G.; Huang, J.; Lieber, C. M. *Nature* **2007**, *449*, 885–890.
- (5) Morales, A. M.; Lieber, C. M. *Science* **1998**, *279*, 208–211.
- (6) Zhang, Y. F.; Tang, Y. H.; Wang, N.; Yu, D. P.; Lee, C. S.; Bello, I.; Lee, S. T. *Appl. Phys. Lett.* **1998**, *72*, 1835–1837.
- (7) He, R. R.; Yang, P. D. *Nat. Nanotechnol.* **2006**, *1*, 42–46.
- (8) Khang, D. Y.; Jiang, H. W.; Huang, Y.; Rogers, J. A. *Science* **2006**, *311*, 208–212.
- (9) Wang, Z. L.; Song, J. H. *Science* **2006**, *312*, 242–246.
- (10) Wang, X. D.; Song, J. H.; Liu, J.; Wang, Z. L. *Science* **2007**, *316*, 102–105.
- (11) Qin, Y.; Wang, X. D.; Wang, Z. L. *Nature* **2008**, *451*, 809–813.
- (12) Yip, S. *Scr. Mater.* **2001**, *45*, 1233–1238.
- (13) Wu, B.; Heidelberg, A.; Boland, J. J. *Nat. Mater.* **2005**, *4*, 525–529.
- (14) Chen, C. Q.; Zhu, J. *Appl. Phys. Lett.* **2007**, *90*, 043105(1–3).
- (15) Yu, M. F.; Files, B. S.; Arepalli, S.; Ruoff, R. S. *Phys. Rev. Lett.* **2000**, *84*, 5552–5555.
- (16) Zhang, Y. F.; Han, X. D.; Zheng, K.; Zhang, Z.; Zhang, X. N.; Fu, J. Y.; Ji, Y.; Hao, Y. J.; Gou, X. Y.; Wang, Z. L. *Adv. Funct. Mater.* **2007**, *17*, 3435–3440.
- (17) Paulo, A. S.; Arellano, N.; Plaza, J.; He, R.; Carraro, C.; Maboudian, R.; Howe, R. T.; Bokor, J.; Yang, P. D. *Nano Lett.* **2007**, *7*, 1100–1104.
- (18) Hsin, C. L.; Mai, W.; Gu, Y.; Gao, Y.; Huang, C. T.; Liu, Y.; Chen, L. J.; Wang, Z. L. *Adv. Mater.* **2008**, *20*, 1–5.
- (19) Heidelberg, A.; Ngo, T.; Wu, B.; Phillips, M. A.; Sharma, S.; Kamins, T. L.; Sader, J. E.; Boland, J. J. *Nano Lett.* **2006**, *6*, 1101–1106.

- (20) Li, W.; Kalia, R. K.; Vashishta, P. *Phys. Rev. Lett.* **1996**, *77*, 2241–2244.
- (21) Godet, J.; Pizzagalli, L.; Brochard, S.; Beauchamp, P. *Phys. Rev. B* **2004**, *70*, 054109(1–8).
- (22) Makeev, M. A.; Srivastava, D. *Phys. Rev. B* **2006**, *74*, 165303(1–7).
- (23) Wang, Z.; Zu, X.; Gao, F.; Weber, W. J. *Appl. Phys. Lett.* **2006**, *89*, 243123(1–3).
- (24) Han, X. D.; Zheng, K.; Zhang, Y. F.; Zhang, X. N.; Zhang, Z.; Wang, Z. L. *Adv. Mater.* **2007**, *19*, 2112–2118.
- (25) Han, X. D.; Zhang, Y. F.; Zheng, K.; Zhang, X. N.; Zhang, Z.; Hao, Y. J.; Gou, X. Y.; Yuan, J.; Wang, Z. L. *Nano Lett.* **2007**, *7*, 452–457.
- (26) Han, X. D.; Zhang, Z.; Wang, Z. L. *NANO* **2007**, *2*, 1–23.
- (27) Landau, L. D.; Lifshitz, E. M. *Theory of Elasticity*; Pergamon Press: New York, 1986.
- (28) Menon, M.; Srivastava, D. *Phys. Rev. B* **2004**, *70*, 125313 (1–6).
- (29) Godet, J.; Brochard, S.; Pizzagalli, L.; Beauchamp, P.; Soler, J. M. *Phys. Rev. B* **2006**, *73*, 092105(1–3).
- (30) Poncharal, P.; Wang, Z. L.; Ugarte, de Heer, W. A. *Science* **1999**, *283*, 1513–1516.
- (31) Loidl, D.; Paris, O.; Burghammer, M.; Riekel, C.; Peterlik, H. *Phys. Rev. Lett.* **2005**, *95*, 225501(1–4).
- (32) Pizzagalli, L.; Beauchamp, P. *Philos. Mag.* **2004**, *11*, 729–736.

NL9012425